Lab on a Chip

Accepted Manuscript

ROYAL SOCIETY OF CHEMISTRY

www.rsc.org/loc

TOC

A novel microfluidic device for the generation of liquid jets with micrometer diameters is described. The gas sheath design allows reliable jetting at highly sample-efficient flow rates under atmospheric and vacuum conditions. The soft-lithographic device fabrication is easy, reproducible and allows the integration of additional features such as a jet-in-jet.

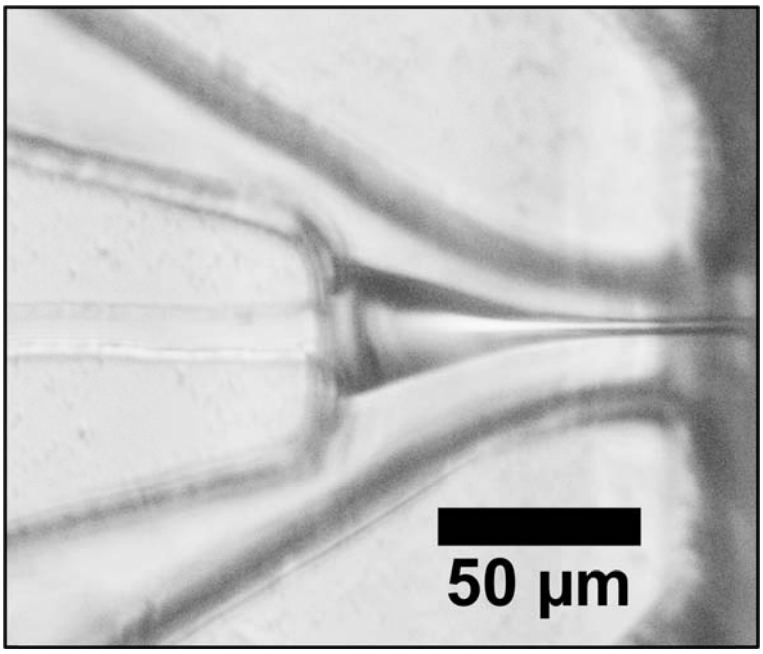

Cite this: DOI: 10.1039/c0xx00000x

www.rsc.org/loc

PAPER

Microfluidic Liquid Jet System with compatibility for atmospheric and high-vacuum conditions†

Martin Trebbin,[a] Kilian Krüger,[a] Daniel DePonte,[b,c] Stephan V. Roth,[d] Henry N. Chapman,[c] and Stephan Förster*[a]

Received (in XXX, XXX) Xth XXXXXXXXX 20XX, Accepted Xth XXXXXXXXX 20XX
DOI: 10.1039/b000000x

We present microfluidic chip based devices that produce liquid jets with micrometer diameters while operating at very low flow rates. The chip production is based on established soft-lithographical techniques employing a three-layer design protocol. This allows the exact, controlled and reproducible design of critical parts such as nozzles and the production of nozzle arrays. The microfluidic chips reproducibly generate liquid jets exiting at perfect right angles with diameters between 20 µm and 2 µm; under special circumstances even down to 0.9 µm. Jetting diameter, jet length, and the domain of the jetting/dripping instability can be predicted and controlled based on the theory for liquid jets in the plate-orifice configuration described by Gañán-Calvo *et al.* Additionally, conditions under which the device produces highly reproducible monodisperse droplets at exact and predictable rates can be achieved. The devices operate under atmospheric and under vacuum conditions making them highly relevant for a wide range of applications, for example at free-electron lasers. Further, the straightforward integration of additional features such as a jet-in-jet is demonstrated. This device design has the potential to integrate more features based on established microfluidic components and become a standard device for small liquid jet production.

Introduction

The generation of liquid jets with diameters in the micron- or sub-micron range is of high relevance in many technologies such as microfiber spinning,[1-7] inkjet printing,[8-10] and the microanalytical dosing of liquids, [11,12] mostly applied for pharmaceutical formulations[13,14] and in microbioanalytics.[15,16] A very challenging example of the latter is its use at free electron lasers (FEL) to provide sub-micron diameter liquid jets for femtosecond X-ray nanocrystallography.[17,18] The enormous intensity of the X-ray pulses at FELs demands a continuous stream of fresh sample, in some cases also at high vacuum conditions, which can be realized by the generation of very small liquid jets that consume only very small amounts of sample over time.

Thin liquid jets can be generated based on the principles of hydrodynamic focusing using gas sheaths developed by Gañán-Calvo *et al.*[19-22] Microjets can also be realized by other techniques such as high-pressure liquid flows or electric fields (electro-spinning).[1,3,5]

The success of pressurized gas systems is based on the gas dynamic virtual nozzle (GDVN)-principle where the liquid enters a volume which is completely filled with pressurized gas that is moving towards the nozzle's exit. This gas flow controls the liquid's shape and flow, forming a continuous liquid jet that is smaller than the liquid inlet geometry and that exits the nozzle without wall contact. Hence, nozzle clogging is essentially eliminated as an experimental concern and sub-10 µm jets and droplets will only be feasible using the GDVN-principle.[5,23,24]

Further, the underlying physics of the GDVN-principle is well understood which helps to create devices that allow resilient jetting of a wide range of liquid samples with only very little consumption of sample over time.[14,25-31] As an example, recent publications show that sub-micrometer liquid jets at flow rates around 75 µl h^{-1} are possible using this principle.[32,33] This high efficiency of sample consumption for the generation of continuous liquid jets is a key element for microanalytical applications.[17,34-37]

Current realizations of pressurized gas devices for the generation of liquid jets use either a plate-orifice configuration or co-axial glass capillaries[5,23] of which the latter are particularly used for free electron lasers.[17,19,23,24,29,35-48] A recent publication also describes a hybrid GDVN-design that incorporates glass-capillaries within a microfluidic channel structure, but the liquid jets are only generated within the closed channel geometry.[24]

The production of such glass capillaries requires complex production steps such as flame polishing, careful alignment of the inner and outer glass capillaries, and final grinding of the tip.[23,24,29,32,44,49,50] The jetting capability can only be assessed after fabrication, thus limiting the production efficiency. Although FEM-simulations have been performed to predict jetting performance in glass capillary nozzles,[32] variations in nozzle dimensions during manufacturing can lead to deviations from the targeted design. This complex fabrication process and complicated geometry control currently limits their availability. Alternatives which satisfy the raising demand for such liquid jet delivery systems are greatly required. Further, there is a great need to implement additional features such as micromixers or

nozzle arrays for advanced multi-functional automated sample delivery.

Microfluidics has become a powerful technology for the handling and manipulation of very small fluid volumes. Devices are easy to fabricate and can contain components for mixing,[51-54] sorting,[55-59] monitoring,[60,61] injecting,[62-66] and many other applications.[67-72] Especially the development of microfluidic devices as an experimental sample environment for (microfocus) X-ray experiments have made enormous progress in the recent years.[73-88] These devices are designed for X-ray transmission measurements in closed microchannels. With the advent of high-intensity sub-micron X-ray beams many devices are not useful because of beam degradation and high X-ray background of the chip materials in the beam. Here micro liquid jets, produced by established microfluidic technology would be highly desirable.

There have been only few examples of microfluidic devices that were used for the generation of free liquid jets.[89,90] These devices have been optimized to perform fast mixing experiments at 3rd generation synchrotron sources based on hydrodynamic focusing at very high flow rates. As a consequence, the devices will operate in the jetting regime, but require samples that are available in sufficient amounts. Another approach to deliver samples in mid-air could be the use of sprays using microfluidic spray dryers that are designed for drug formulation.[89-91]

In this paper we present the development, fabrication and testing of easy-to-build microfluidic micron-size liquid jet devices which run essentially clogging-free due to their GDVN-based design.[23] Further, these devices are capable to operate under atmospheric and vacuum conditions making them compatible with evacuated sample environments. For the device production we developed a three-layer soft-lithography protocol that allows the efficient and reproducible fabrication of microfluidic liquid jet devices that incorporate arrays of multiple jet-nozzles on each single chip. The capability to predict jetting characteristics is demonstrated by the comparison of experimental data using a high speed camera with theoretical models and is underlined by additional 3D finite-element-based CFD-simulations of the given nozzle design. Further, we show the potential of sub-micrometer jetting under vacuum conditions and demonstrate, with the example of a jet-in-jet system, the possibility to integrate more complicated design structures into the microfluidic device without the need of additional production steps.

Device production

Microfluidic soft lithography. The microfluidic liquid jet devices are fabricated using established soft lithography techniques.[92-96] This process can be seen as a two-part sequence.

The first part is about creating a microstructured master which will then be used as a molding template in the second part of the device fabrication routine. This master can be created relatively fast which enables rapid prototyping due to the use of established SU-8-based photolithographic procedures. Further, this master can be re-used multiple times in the subsequent fabrication process.

The second part of the fabrication process can be performed easily and a large number of nozzle geometries can be replicated with each single mold. The molding and device sealing steps only require minimal equipment, which should help to migrate the microfluidic liquid jet technology to a wide range of users. An overview of this process is illustrated in Fig. 1 while further details are outlined in the next paragraph and the experimental section.

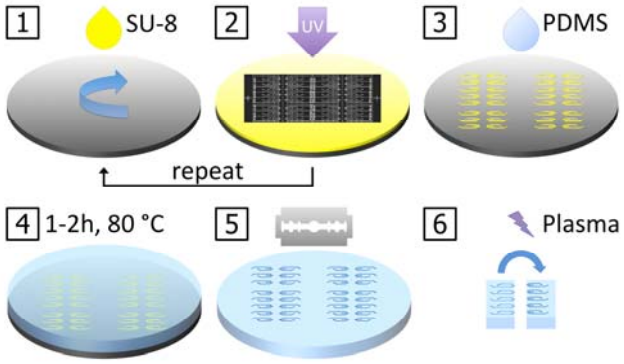

Fig. 1 Soft lithographic fabrication sequence for microfluidic liquid jet devices. The photolithographic master fabrication involves repeating steps to build up a multilayered microstructure: spin-coating (1) and UV-exposure (2). After development, the uncured photoresist is removed and the resulting microchannel template is replicated using polydimethylsiloxane (PDMS; 3,4). The replica is peeled off the master device and inlet ports for fluids are added. The polymer is cut using a razor blade (5) and the device is sealed using air plasma treatment (6).

Microfluidic liquid jet device fabrication. The integration of the GDVN-principle into the microfluidic chips is realized by fabricating 3D-microchannels that are replicated from multilayered SU-8-microstructures on a polished silicon wafer. The underlying photolithographic sequence for the creation of these multilayered templates involves repeating cycles of spin coating the photo resist, photo mask alignment and UV exposure. In this process, the layer combinations A+B+C or B+C are exposed onto the photoresist to create the desired nozzle geometries, as illustrated in Fig. 2.

Next, the master structure is replicated with polydimethylsiloxane (PDMS) which, in a single molding step, yields the upper and lower halves of the three-dimensional microchannels. Scanning electron micrographs of these PDMS-nozzle geometries are shown in Fig. 2 while their exact dimensions are summarized in Tab. 1.

Prior to the alignment and sealing of these PDMS-halves, the microfluidic liquid jet device fabrication requires to cut off excess PDMS next to the nozzle tips with a razor blade. This cutting position is indicated by a red dotted line in Fig. 2. It is important to note that the jet nozzles are solely shaped by the lithographically created microstructures and will not be touched by the blade. This is ensured by the integration of the third C-layer which acts as a spacer- or sacrificial layer at the nozzle tip. It protects the function and integrity of the nozzle, ensures easier cutting and also acts as an optical guide for the eye. Since X-ray beams will hit the liquid jet in close proximity to the microfluidic device, the range of observable scattering angles (at high q) depends on the microfluidic design itself and the razor blade cutting angle. Consequently, the observable q-range can be easily

extended by tilting the razor blade accordingly.

The last step involves the exact alignment and plasma-activated sealing of this pair of PDMS-microchannel halves. The precise alignment is achieved by additional multilayered orientation structures next to the main nozzle geometries. These guiding pairs of 3D-microstructures have already been included in the above photolithographic steps and, now, facilitate the necessary alignment almost automatically by snapping into each other. This results in well-centered microchannels and liquid jets that exit the microfluidic nozzle in a straight line at perfect right angles. A photograph of the final PDMS-device including the attached tubing, as well as a microscopic image of the nozzle during operation, are shown in Fig. 3.

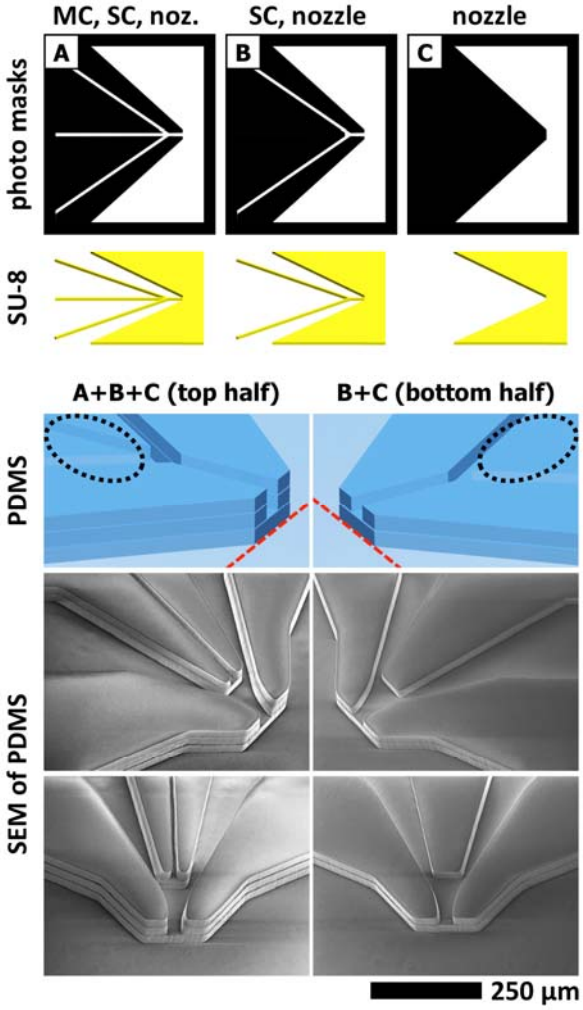

Fig. 2 Illustration of the multilayer principle for the creation of 3D microfluidic liquid jet nozzle arrays (aperture-less nozzle version). (A-C) Representation of the individual emulsion film masks (top) and their resulting structured SU-8 layers (middle). These are combined differently to create multilayered SU-8 structures which are replicated using PDMS (bottom). Illustrations and scanning electron microscopic images show the upper (bottom left) and lower (bottom right) PDMS halves of a 3D nozzle prior to the subsequent device bonding steps. The B-layer can include a blocking element at the nozzle tip (nozzle version with aperture) to reduce the outlet cross section for smaller jets and lower gas flows (see Supplemental Information).

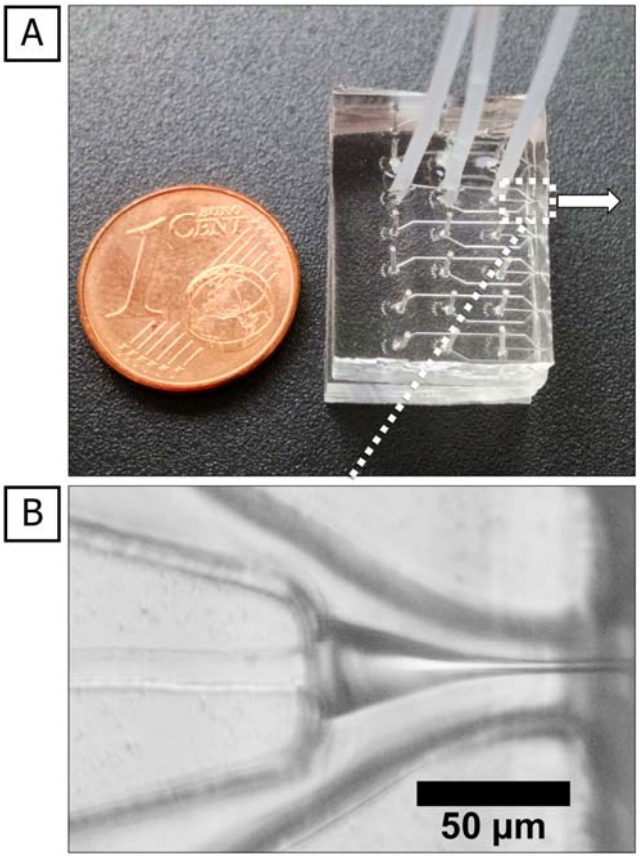

Fig. 3 (A) Photograph of the final microfluidic device with an array of liquid jet nozzles that can be operated individually or in parallel. (B) Light microscopic image of one microfluidic nozzle during operation. The liquid in the central channel is focused with pressured air which enables stable liquid jets with small diameters at low sample flow rates while it runs essentially clogging-free due to this air sheath. The microfluidic liquid jet devices operate well under atmospheric pressures and under vacuum conditions.

Nozzle design. The benefit of using soft-lithography-based microfluidics for the generation of liquid jets lies in the high reproducibility of microstructures and the precise control over very small features in the µm-range. As a result, the liquid inlet is perfectly centered and the jet exits the nozzle's outlet in a straight line. The microfluidic liquid jet devices are designed using the software AutoCAD that allows controlling the design parameters of the nozzle geometry that directly determine the conditions for liquid jetting. This microfluidic nozzle design and the design parameters definitions are presented in Fig. 4 and the following Tab. 1.

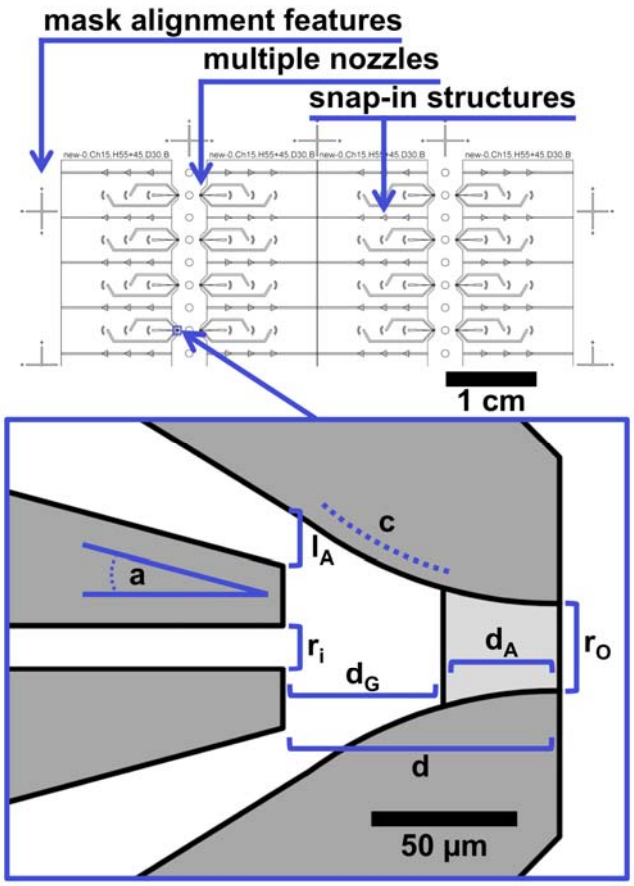

Fig. 4 Nozzle design parameters. (Top) Excerpt of a CAD drawing which contains features for aligning the mask during the photolithographic process and snap-in structures for the later replica alignment during the device fabrication. (Bottom) An illustration of the controllable design parameters is depicted below. These features can be adjusted with high precision and reproducibility to fine-tune the jetting behavior of the desired liquid.

Nozzle arrays. The master structures can contain multiple dense nozzle arrays on a single device which are replicated simultaneously with each molding step. The resulting nozzles can be operated individually or in parallel. Next to the possibility of massive parallelization of nozzles, the integration of dense nozzle arrays on a microfluidic chip also allows to maintain a very small device footprint. The current microfluidic designs contain adjacent liquid jet nozzles every 3.3 mm which could also be reduced easily.

Disposable chips. The effectiveness and ease of the production process allows even to fabricate disposable microfluidic liquid jet devices in large numbers. The use of such disposable liquid jet devices can be of great advantage when hazardous or toxic samples like virii, bacteria, bio-active compounds or nanoparticles need to be handled.

Tab. 1 List of microchannel design parameters and their definitions along with relevant parameter combinations and ratios.

Design Parameter	Definition
r_O	width at the outlet (30 µm)
r_i	width of the main channel (15 µm)
d	distance from main channel inlet to nozzle outlet (95 µm)
d_G	distance of the gap between main channel inlet (55 µm)
d_A	distance of the aperture (40 µm)
l_A	length of the air inlet (20.4 µm)
a	angle of the air stream (15 °)
c	curvature of the tapering (144.3 µm arc radius)
not shown in the illustration:	
h_n	height of layer n (30 µm)
extra aperture	presence of an aperture at top and bottom layer of the nozzle outlet
Relevant design parameter ratios	
r_o : d	d_G : d_A
r_i : r_o	l_A : r_i :l_A
(r_i+2*l_A) : r_o	(r_i+2*l_A) : d
a : d	c : d

Results and Discussion

Design control and performance. The microfluidic chips reliably produce stable liquid jets, using aqueous solutions in our case, with typical diameters in the lower µm-range that can be controlled precisely. The 3D design gives the option to incorporate additional obstacles at the top and bottom of the 3-layered microchannel's exit, reducing the cross section of the aperture to a fraction, depending on the individual layer heights. Further, this aperture integration also reduces the gas flow (see Supplemental Information) and the generated jets are generally smaller in diameter, exit at higher velocities, and the stable jetting requires lower minimal liquid flow rates than their aperture-less analogues. We studied the microfluidic liquid jetting behavior in this enhanced version of the nozzle at atmospheric ambient pressure and the results are shown in Fig. 5.

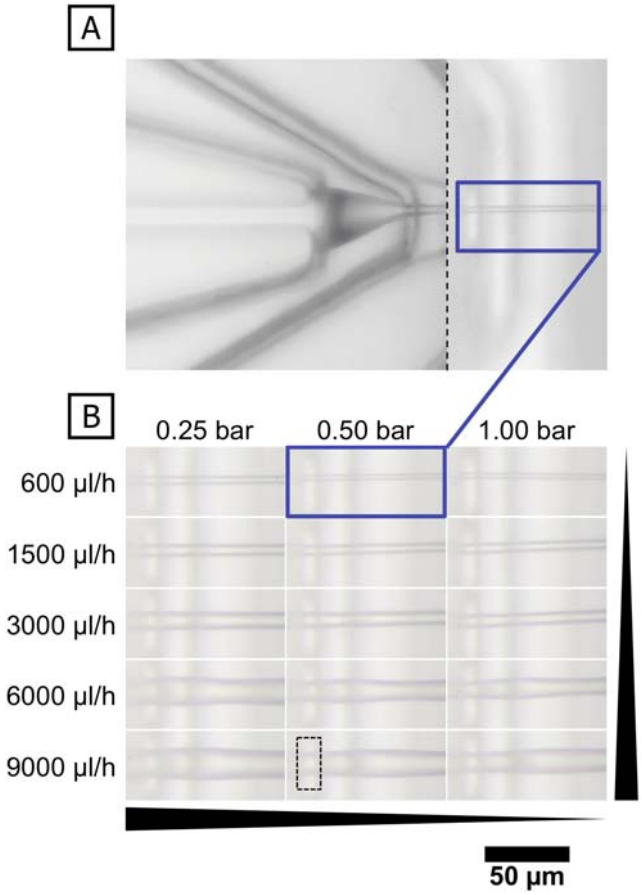

Fig. 5 Jet diameter control visualized by microscopic images of the microfluidic liquid jet nozzle during operation. (A) The water enters the nozzle and is shaped by the pressured air flow and the geometric device design. This results in a constant and stable liquid jet. The top image is merged from two frames at different focus positions due to the optical distortion of PDMS and is indicated by a dotted line. (B) The change of jet diameters at varying conditions is shown below and was measured directly at the nozzle outlet. The black dotted rectangle marks the region of the jet diameter measurements while the stretched black triangles indicate the trends of increasing or decreasing liquid jet diameters.

Jet diameter control. The jet at the outlet of the liquid jet nozzle is imaged to analyze the relation between its diameter and the applied experimental parameters. We observe the trend that lower liquid flow rates and increased gas pressures both lead to smaller jet diameters as shown in Fig. 5. In this image series at atmospheric ambient pressure, the flow rates were varied between 600 µl h^{-1} and 9000 µl h^{-1} at compressed air pressures between to 0.25 bar and 1.00 bar which results in jet diameters between 3.5 µm and 19 µm. Assuming that the well-studied plate-orifice configuration and this microfluidic liquid jet system share the same underlying physics, we apply the model described by Gañán-Calvo *et al.* which describes the liquid jet diameter d_j:[19,26,97-99]

$$d_j \simeq \left(\frac{8\rho_l}{\pi^2 \Delta p_g} \right)^{1/4} Q^{1/2} \quad (1)$$

with the density of the liquid ρ_l, the pressure difference Δp_g and the flow rate Q. For best reproducibility, the jet diameter is measured manually using ImageJ at multiple positions directly next to the nozzle exit (see indication in Fig. 5). We find that this theoretical model and the experimental results are in very good agreement for almost all flow rates, as shown in Fig. 6A. The measured diameters only start to deviate from the predicted values at high flow rates (≥ 6000 µl h^{-1}) which might originate from the curved surface instabilities that modulate the liquid jet diameter downstream, as shown in Fig. 5.

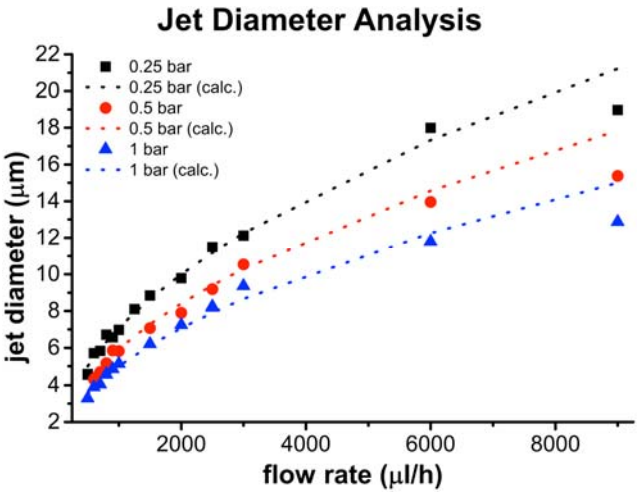

Fig. 6 Comparison of experimental data with theoretical predictions regarding jet diameter and breakup transition analysis. The jet diameter at different flow rates and applied pressures with a controllable jet diameter between 3.5 µm and 19 µm.

Controlled droplet breakup. The liquid jets exit the microfluidic devices at velocities in the range of tens of m/s and the droplet breakup consequently appear as a thin blurred line to the eye. Therefore we studied the jetting behavior and droplet breakup of a water jet using a high speed camera at 2 µs exposure times and frames rates of ca. 15,000 fps, using the aperture-less nozzle design for lower droplet velocities to ensure sharper images. The required high speed video setup is described in more detail in the experimental section while the resulting images are shown in Fig. 7. The droplet breakup is studied at a constant air pressure of 0.25 bar while the liquid flow rate was varied to study its influence on the breakup characteristics.

The high speed camera frames reveal that an increasing flow rate leads to larger droplets with an increase from 8.7 µm at 500 µl h^{-1} to 29.8 µm at 9000 µl h^{-1}. Further, the length of the continuous jet, before it breaks up into droplets, increases from 137 µm to 867 µm over the same flow rate interval. This has important implications for the integration of microfluidic liquid jet devices at X-ray sources because the length of the uninterrupted liquid stream dictates the proximity of the X-ray beam to the nozzle at a given flow rate.

Further, this high speed video setup allows the experimental classification of the droplet breakup type. The breakup of a liquid jet leads to the formation of drops due to the downstream growth of axisymmetric capillary waves (the Rayleigh instability [100]) that are commensurate with the jet diameter. The different possible droplet breakup types that can be identified are described in more detail elsewhere and will be covered only briefly.[28,75,101,102] (I) The jetting state shown in Fig. 7B corresponds to the first type, which is globally and locally stable (GS/LS). Here, the liquid meniscus is stable inside the nozzle and the liquid exits the orifice

as a continuous column because the growing axisymmetric perturbations are swept away downstream (convectively unstable [103] (II) Unstable states, such as spraying, where the tapering liquid meniscus is unstable, can be observed at increasing pressures for a given liquid flow rate and they correspond to the global and local instability (GI/LI). (III) The third parameter domain corresponds to a globally stable, but locally instable jetting regime (GS/LI). Here, the liquid meniscus is stable inside the nozzle geometry, as shown in Fig. 7C, but the jet breaks up into a continuous droplet stream because the growing perturbations travel upstream and pinch off the interface close to the orifice (absolutely unstable [103] This GS/LS- to GS/LI-transition lies in the range of the Leib-Goldstein limit that predicts the convection/absolute instability transition.[101,102,104] The GS/LI-state can be reached by starting with stable jetting (GS/LS, case I) and then lowering the pressure (>0.1 bar) at a given liquid flow rate (3000 µl h^{-1}). Under these conditions a homogenous stream of equidistant drops (135 µm) with a diameter of 50.5 µm can be observed at a constant rate (ca. 12.36 kHz). If the pressure, at this given flow rate, is decreased even further towards 0 bar, the jetting collapses (GI/LI, case II).

These findings and the predictable jet diameters are particularly interesting because they suggest that the knowledge and theories about the well-studied plate-orifice- and GDVN-designs can be applied to the microfluidic liquid jet devices as well. This helps tremendously with the theoretical prediction of jetting behavior as well as the development of future optimized devices. Further, this principle could potentially be used to generate small droplets at a constant and controllable rate if the flow rates and other relevant experimental parameters are adjusted accordingly. This possibility could be interesting for applications that require synchronization of homogenous droplet streams to a certain frequency.

CFD-based jet optimization. It is possible to analyze further design details on the jetting behavior using established computational fluid dynamic (CFD)-simulations that allow the microchannel design to be adjusted accordingly in AutoCAD. This combination of precise fabrication control and CFD-simulations is known as computer-aided rapid prototyping.[80,93,105]

As an example, the jetting behavior of a water jet in air is simulated with the CFD-software package COMSOL using a time-resolved Newtonian two-phase model. First, the microfluidic nozzle geometry is imported from the CAD- into the CFD-software and the boundary conditions, such as inlets, outlets, etc., are set as described in further detail in the Supplemental Information. We choose a time-resolved model because the initial fluid interface is a flat plane, between the inlet channel and the gas flow volume, which then evolves to the stable liquid jet that is shown in blue in Fig. 8. Due to the complexity of this 3D model, symmetry of the microfluidic liquid jet nozzle was taken into account which enables to consider the geometry's full 3D shape while only modeling its top right quarter. This reduced the amount of necessary finite elements and allowed us to increase the modeling quality of the liquid jet. These detailed finite element meshes are shown in Fig. S1 of the Supplemental Information.

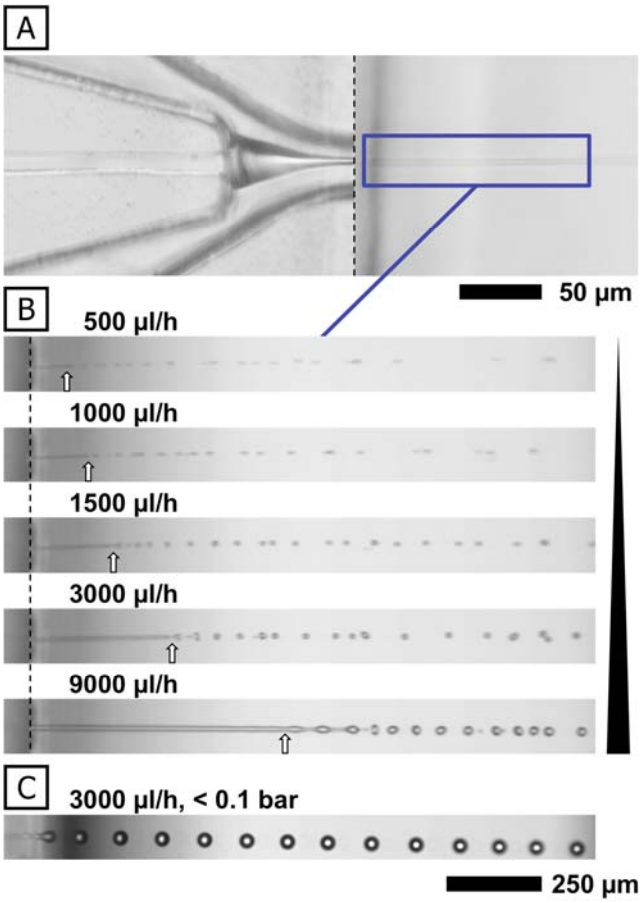

Fig. 7 Controlled droplet break-up. (A) Light microscopic image of a microfluidic liquid jet device that focuses a water jet with pressured air (GS/LS). (B) High speed camera frames (2 µs exposure, ca. 15,000 fps) of the jetting lengths, with the black dotted line marking the zero position, and droplet breakup (global and local stability) at flow rates between 500 µl h^{-1} and 9000 µl h^{-1} at a pressure of 0.25 bar (global instability transition) and (C) Rayleigh breakup (global stability, local instability) in the same device at lower pressures (< 0.1 bar) and a flow rate of 3000 µl h^{-1}. The highly constant droplet-frequency and -size can be adjusted by changing the experimental parameters, such as pressure or flow rate.

This CFD-simulation of a liquid jet is an example for future similar models that can be used to optimize the system, gain important insights into the 3D liquid jet shape and understand its dynamics under different conditions because the CFD-model considers the exact geometry of the microfluidic nozzle which can be fabricated reproducibly using soft lithography.

The CFD-simulations clearly show that the resulting liquid jet is shaped by the interplay of microchannel geometry and the compressed air at high velocities. We performed the simulation of the water liquid jet for the same parameters as the experiment: with a water flow rate of 600 µl h^{-1} and air at a pressure difference of 0.25 bar. As a verification of the CFD-model, the simulation results are compared to the experimental high speed video data under these exactly same conditions and we find that the results are in very good agreement, as shown in Fig. 8A. Further, the color-coded flow lines in this figure indicate the pressure drop which results from the volume expansion when the air from the side channels enters the bigger volume where the fluid focusing occurs. The compressed air expectably shapes the

liquid jet not only from the sides, but also from top and bottom according to the GDVN-principle which prevents any contact of the liquid to the nozzle wall and yields a very small liquid jet diameter at the nozzle outlet.

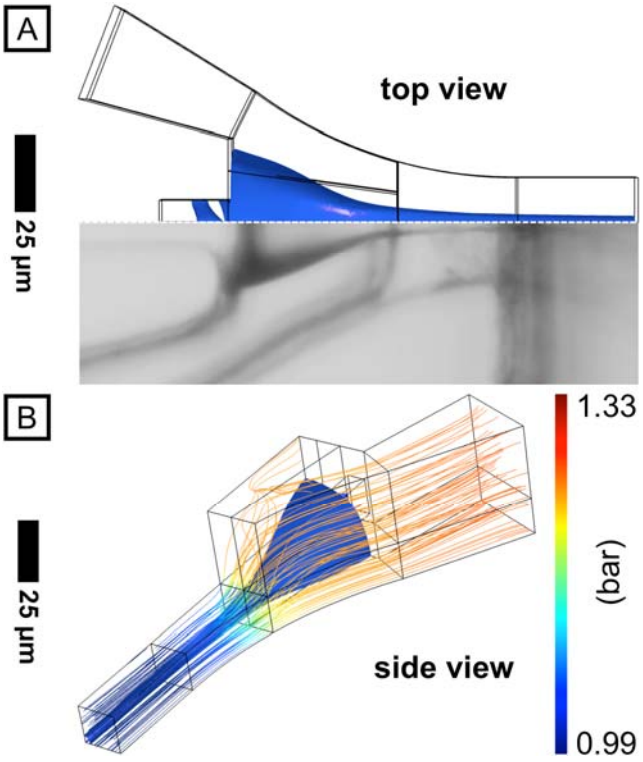

Fig. 8 3D CFD-simulation results compared to the experimental data under the same conditions: water jet in air at a flow rate of 600 µl h^{-1} with a pressure difference of 0.25 bar. (A) Top view on the 3D simulation the corresponding light microscopic image shows the good agreement between the theoretical and experimental jet shape. (B) Side view on the 3D shape of the liquid jet where the blue shape represents the interface between the two simulated fluid phases of water and air. The streamlines are color-coded to show the pressure gradient in the focusing area.

Vacuum operation. The microfluidic liquid jet devices operate well under atmospheric ambient pressures or under vacuum conditions. The low gas flow rates are measured experimentally and should allow a vacuum in the range of 10^{-6} bar, as described in further detail in the Supplemental Information. To demonstrate the stable jetting behavior under vacuum conditions, we performed tests in a scanning electron microscope (SEM, EVO LS, Carl Zeiss AG) using a microfluidic liquid jet device and water as a liquid sample. The SEM is operated at a chamber pressure of < 10 mbar and the liquid- and air-flows are pumped by applying adjustable pressures. The flow rates are monitored in situ using a micro-volume flow meter (Sensirion AG). The observed jet diameters typically were in a range of 2 µm to 4 µm at flow rates between 150 µL h^{-1} and 1000 µl h^{-1} and pressures up to 3 bar.

An example SEM image of a liquid jet in a microfluidic device in operation is depicted in Fig. 9. The device runs at the low flow rate of 150 µL h^{-1} at an air pressure of 1.7 bar yielding a stable liquid jet with a diameter of 2.46 µm. After a short, unintentional high overpressure burst, we observed a stable microfluidic liquid jet with a sub-micron diameter (940 nm) at an even lower flow rate of 135 µl h^{-1} at an applied pressure of 1.9 bar. This observation indicates the optimization potential of this microfluidic liquid jet system. We suspect that the d/r_0-ratio (see Fig. 4) changed in this event because this ratio is known to have a sensitive effect on the lowest minimal flow rate.[27]

These vacuum conditions in the SEM sample chamber mimic the conditions that are typically found in the sample chambers at free electron lasers. Combined with the low liquid flow rates, this compatibility makes the microfluidic liquid jet device a suitable alternative to current sample environments.

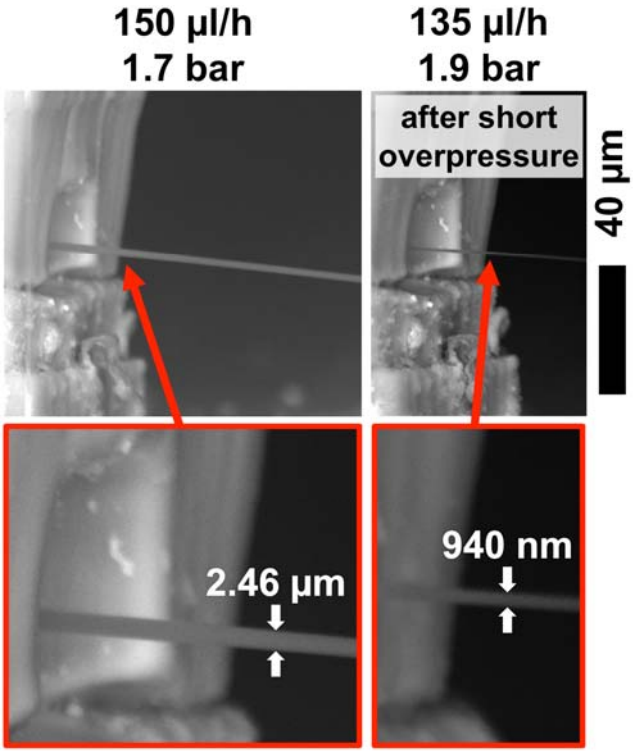

Fig. 9 Liquid jetting under vacuum conditions. Scanning electron microscopic (SEM) image of microfluidic liquid jet device during operation under vacuum conditions. The liquid jet (pure water) exits the nozzle as a straight continuous sample stream while its GDVN-based design enables essentially clogging-free stable jetting with small diameters at low sample flow rates. By regulating pressure and sample flow rates, the jet diameter can be adjusted.

Sample consumption and -compatibility. Due to the air-focusing design, the here presented microfluidic liquid jet devices can be operated at very low sample consumption rates which is highly important for solutions of scarce valuable samples such as proteins. The current minimum flow rates for stable jetting are typically in the range of the commonly used glass capillaries (135 to 500 µl h^{-1}).[17,32,106] Ongoing studies indicate that these minimal flow rates for stable jetting can be further decreased by adjusting the design parameters, like channel-shapes, -heights, -dimensions and aspect ratios, according to the sample's individual fluid properties.

The GDVN-based design typically results in the very reliable and continuous generation of liquid jets which are resilient to a wide range of experimental conditions; both for microfluidic devices and glass capillaries. However, there are extreme examples of samples where the GDVN-design is stretched to its limits. This is the case for highly viscous samples or solutions that contain high concentrations of salts because solution

components tend to plate out at the periphery of this wetted region and eventually grow back to occlude the capillary exit or alter the gas flow. In case of glass capillaries, this problem can be overcome by forming micrometer-sharp edges on the front of the liquid capillary.[24] While the side edges of the microfluidic liquid inlet channel can be fabricated with a similar sharpness, to reduce the wetted area, the edge at the top and bottom remain rather flat. However, this wetted region can be minimized even further by using established surface treatments, such as Aquapel™- or parylene-coating, which have been successfully used against device fouling. [107-109]

To demonstrate the wide sample compatibility of *untreated* microfluidic liquid jet devices, the chips are tested with different solutions that are examples for commonly used protein crystallization buffers and which contain high concentrations of poly(ethylene glycol) and salts. The microfluidic liquid jet devices operate error free and without any indication of clogging for a period of 60 min after which the experiment is *intentionally* stopped (see Supplemental Information).

Solvent compatibility. PDMS is compatible with aqueous and polar solvents, and thus suitable for most biological or protein samples.[106,110,111] For use with nonpolar solvents, coating procedures based on established PDMS surface chemistry, e.g. borosilicate glass or fluorinated repellant coatings, have been demonstrated [89,92,94,96,106]. Further, the described device fabrication procedures can be transferred to other elastomer materials and other microfluidic production techniques such as (hot) soft embossing, including materials such as Teflon® [97-99] Kapton®,[75] THV®,[104] COC/TOPAS®,[80] PS,[106] PE,[106] PMMA,[89,106] NOA81,[112,113] glass[114] and silicon.[114] Combined with the here-described integrated snap-in structure for device alignment, this enables the use of a broad range of solvents in microfluidic liquid jet devices. Production techniques such as (hot) soft embossing or micro injection molding also open the path to industrial large scale productions with the possibility to mass-produce disposable devices.

Integration of additional features. The soft lithography-based liquid jet device production allows the integration of additional features or microfluidic building blocks without any additional processing steps. Available microfluidic building blocks include design concepts for simple functions like i.e. mixing, sorting, measuring, injecting, switching or droplet- and microparticle-generation, which can be stacked to build up complex chip-labs. A prominent example of stacked, simple elements that perform complex tasks is the concept of microfluidic large scale integration by Quake *et al*. which includes pumps,[115] valves[116] and multiplexers.[71] This building block concept enables the sample handling and fluid manipulation within the microfluidic liquid jet device and opens up many new opportunities for liquid jets.

Jet-in-jet. As an example for the integration of microfluidic tools into the liquid jet device, we demonstrate the fabrication of a jet-in-jet geometry that focuses two liquids hydrodynamically into a gas-focused jet of the combined liquids. Hydrodynamic flow focusing and its combination with a coaxial gas flow using capillaries has been described before, [22,51] but each additional liquid stream inside a liquid stream requires additional working steps due to the capillary-based design. In this soft lithography-based example however, mixing geometries are handled as individual microfluidic building blocks of which one or many can be simply added to the existing GDVN-nozzle design with high precision and reproducibility; without the need of any additional fabrication steps. This simple combination enables *in situ* mixing experiments within the liquid jet, like i.e. the study of nanoparticle growth,[89,90] the time-triggered dosing of liquids into a stable liquid jet or ultra-fast pump-probe laser experiments.[2,4,6,7,33]

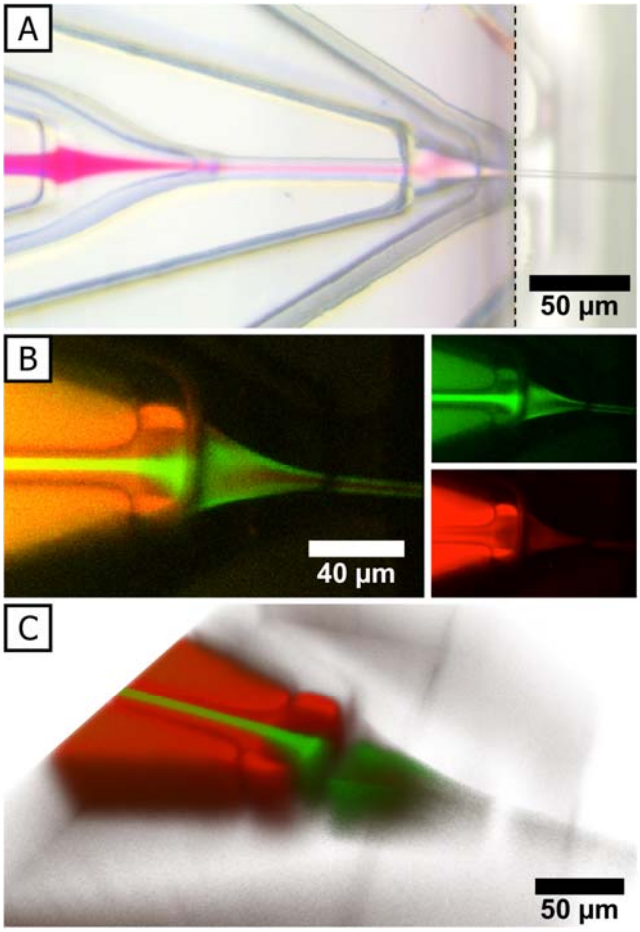

Fig. 10 Jet in Jet. Microscopic images of a microfluidic liquid jet in jet device during operation at 1 bar and a (medium) flow rate of 500 µl h^{-1} for each liquid channel. The flow rate ratio between side and main channels (SC:MC:SC) is therefore 1:1:1. (A) The light microscopic image shows a solution of rhodamine B dye which is focused in pure water before it exits the device as a liquid jet. (B left) Fluorescence image of the liquid jet's cut plane taken with a confocal laser scanning microscope at its center. This is the same device as (A), but it is operated with different dyes which are recorded on individual color channels: fluoresceine (B top right, green channel) and rhodamine B (B bottom right, red channel). An inversion of dyes is observed. (C) A complete stack of confocal cut plane images at different focus positions of this liquid jet has been recorded. The resulting 3D-reconstruction is presented from an inclined top-down view angle.

We demonstrate a microfluidic jet-in-jet device mixing two dyes, fluoresceine and rhodamine B, by hydrodynamic flow focusing which are then focused as a liquid jet using the GDVN-

principle. The pressurized air is adjusted to 1 bar and the liquid flow rate is 500 µl h^{-1} for each liquid channel which results in a flow rate ratio between side and main channels (SC:MC:SC) of 1:1:1. The jetting behavior is imaged using a light microscope (rhodamine B in water) and confocal laser scanning microscopy (fluoresceine in rhodamine B) as shown in Fig. 10.

The green and red fluorescence of these dyes at the center of the liquid jet is recorded on individual color channels of the confocal microscope as shown in Fig. 10B. Additionally, we record a complete stack of confocal cut plane images at different focus positions of this liquid jet enabling a 3D-reconstruction of the liquid jet. The lower half of this resulting 3D-reconstruction is presented from an inclined top-down view angle in Fig. 10C. We observe that the liquid jet is not only focused from the sides but also from top and bottom. This observation and the liquid jet's 3D shape are in good agreement with the CFD simulation results that have been discussed above.

Experimental

Photolithographic Master Fabrication. This part of the fabrication process is performed in a clean room and starts by spin-coating (Cee 200X, Brewer Science Inc.) a 3" silicon wafer with a negative photoresist (SU-8 50, Microchem Co.). This step is illustrated in Fig. 1.1. The microchannel structures are imparted to the photoresist using a mask aligner (MJB4, Süss MicroTec AG) as shown in Fig. 1.2. The previous steps are repeated to build up two additional layers onto the silicon wafer, as shown in Fig. 2. The uncured photoresist is removed in the subsequent development process which yields a multi-layered master. All relevant process parameters are optimized to obtain microstructured layers with a very uniform height of 30 µm per coating-exposure-iteration. The geometric design parameters of the microchannel are summarized in Tab. 1.

Microfluidic Device Fabrication. The second part of the fabrication process continues under dust-free conditions by replicating this microstructured master using polydimethylsiloxane (PDMS, Sylgard 184 kit, Dow Corning Co.) and curing it for ca. 2 h at 80 °C. These steps are depicted in Fig. 1.3&4. The PDMS replica is removed from the master and inlet ports are punched into the polymer using a biopsy punch needle (Harris Uni-Core™ 0.75 mm). The polymer is cut into smaller pieces for better handling and the excess PDMS next to the outlet nozzles is cut off using a razor blade, as shown in Fig. 1.5. This step is performed under a microscope to ensure high quality. The microchannel design allows preparing several nozzles simultaneously since the replicated structures incorporate an additional PDMS-layer that protects the nozzle's integrity and function during the cutting process (see discussion of Fig. 2). Additionally, cutting in a steeper angle (or adjusting the CAD drawing) will extend the range of coverable X-ray scattering angles. The final array of microfluidic 3D-focused liquid jet nozzles is created by bonding the two halves of PDMS. This is achieved by activating the surface using air plasma (MiniFlecto-PC-MFC, GaLa Instrumente GmbH), adding a little drop of pure water (0.2 µm-filtered Millipore), aligning the structures and drying at 30 °C for ca. 1 h. The use of a microscope will help during the alignment step, but typically the integrated orientation structures of the multi-layer design will snap in and align the microstructures automatically and with high precision.

Microfluidic liquid jet device operation. The microfluidic liquid jet devices operate stably under different conditions. The devices are tested over periods of several hours to demonstrate the long term stability of the system. Syringe pumps (Nemesys, Cetoni GmbH) are connected to the device using PE tubings (Science Commodities Inc.). All tested liquids, such as pure water (Milli-Q, Millipore), are filtered through a 0.2 µm- or 5 µm-PTFE filter prior to use. The experimental conditions include flow rates between 150 µL h^{-1} and 9000 µL h^{-1} at constant pressures between < 0.1 bar and 5 bar. During the startup sequence, the air flow is started first and then adjusted to the desired value. Next, the syringe pumps are started and regulated down to the targeted flow rate for stable jetting. The imaging setup involves an Olympus IX71 inverse microscope and a highly intense, focused light source that allows exposures down to 2 µs. The fast processes, as the droplet breakup or the startup evolution, are recorded using a high speed camera (Phantom v9.1, Vision Research) allowing to capture frames at a rate of 150,000 s^{-1}. The stable jetting behavior is also studied and captured using a DSLR camera (D7000, Nikon) which delivers high resolution images for further analysis.

Conclusions

In conclusion we demonstrate the production of microfluidic chip based devices that produce liquid jets with micrometer diameters while operating at very low flow rates. The chip production is based on established soft-lithographical techniques employing a three-layer design protocol. This allows the exact, controlled and reproducible design of critical parts such as nozzles and the production of nozzle arrays. The microfluidic chips reproducibly generate liquid jets exiting at perfect right angles with diameters between 20 µm and 2 µm; under special circumstances even down to 0.9 µm. Jetting diameter, jet length, the domain of the jetting/dripping instability can be predicted and controlled based on the theory for liquid jets in the plate-orifice configuration described by Gañán-Calvo *et al*. Additionally, conditions under which the device produces highly reproducible monodisperse droplets at exact and predictable rates can be achieved. The devices operate under atmospheric and under vacuum conditions making them highly relevant for a wide range of applications, for example at free-electron lasers. Further, the straightforward integration of additional features such as a jet-in-jet is demonstrated. This device design has the potential to integrate more features based on established microfluidic components and become a standard device for small liquid jet production.

Acknowledgements

We thank the European Research Council for financial support within the ERC Advanced Grant project STREAM (#291211) and the Federal Ministry of Research (BMBF, #05K13WC5). Very helpful discussions with Joachim Schulz (XFEL, Hamburg, Germany), Kenneth Beyerlein and Dominik Oberthür (both CFEL/DESY, Hamburg, Germany) are gratefully acknowledged.

Notes and references

[a] *University of Bayreuth, Physical Chemistry 1, Universitätsstraße 30, 95447 Bayreuth, Germany. Fax: +49(0)921-55-2780; Tel: +49(0)921-55-2760; E-mail: stephan.foerster@uni-bayreuth.de*
[b] *SLAC, Stanford, California, USA.*
[c] *CFEL, DESY, Hamburg, Germany.*
[d] *HASYLAB, DESY, Hamburg, Germany.*

† Electronic Supplementary Information (ESI) available: CFD-simulation details, gas flow quantification. See DOI: 10.1039/b000000x/

1. A. M. Gañán-Calvo, *Journal of Aerosol Science*, 1999.
2. Y. M. Shin, M. M. Hohman, M. P. Brenner, and G. C. Rutledge, *Appl. Phys. Lett.*, 2001, **78**, 1149.
3. A. M. Gañán-Calvo, *Phys. Rev. Lett.*, 1997, **79**, 217–220.
4. A. Greiner and J. H. Wendorff, *Angewandte Chemie International …*, 2007.
5. A. M. Gañán-Calvo and A. Barrero, *Journal of Aerosol Science*, 1999, 1–9.
6. J. E. Díaz, A. Fernández-Nieves, A. Barrero, M. Marquez, and I. G. Loscertales, *J. Phys.: Conf. Ser.*, 2008, **127**, 012008.
7. A. Greiner and J. H. Wendorff, Springer Berlin Heidelberg, Berlin, Heidelberg, 2008, pp. 107–171.
8. B.-J. de Gans and U. S. Schubert, *Macromol. Rapid Commun.*, 2003, **24**, 659–666.
9. S. Hauschild, U. Lipprandt, A. Rumplecker, U. Borchert, A. Rank, R. Schubert, and S. Förster, *Small*, 2005, **1**, 1177–1180.
10. G. D. Martin, S. D. Hoath, and I. M. Hutchings, *J. Phys.: Conf. Ser.*, 2008, **105**, 012001.
11. C. M. Whitehouse, R. N. Dreyer, M. Yamashita, and J. B. Fenn, *Anal. Chem.*, 1985, **57**, 675–679.
12. K. Tang and A. Gomez, *Journal of Colloid and Interface Science*, 1995, **175**, 326–332.
13. S. Agarwal, A. Greiner, and J. H. Wendorff, *Adv. Funct. Mater.*, 2009, **19**, 2863–2879.
14. A. M. Gañán-Calvo and J. M. Montanero, *Phys Rev E Stat Nonlin Soft Matter Phys*, 2009, **79**, 066305.
15. N. Mongkoldhumrongkul, S. Best, E. Aarons, and S. N. Jayasinghe, *J Tissue Eng Regen Med*, 2009, **3**, 562–566.
16. S. N. Jayasinghe, *Analyst*, 2011, **136**, 878–890.
17. H. N. Chapman, P. Fromme, A. Barty, T. A. White, R. A. Kirian, A. Aquila, M. S. Hunter, J. Schulz, D. P. DePonte, U. Weierstall, R. B. Doak, F. R. N. C. Maia, A. V. Martin, I. Schlichting, L. Lomb, N. Coppola, R. L. Shoeman, S. W. Epp, R. Hartmann, D. Rolles, A. Rudenko, L. Foucar, N. Kimmel, G. Weidenspointner, P. Holl, M. Liang, M. Barthelmess, C. Caleman, S. Boutet, M. J. Bogan, J. Krzywinski, C. Bostedt, S. Bajt, L. Gumprecht, B. Rudek, B. Erk, C. Schmidt, A. Hömke, C. Reich, D. Pietschner, L. Strüder, G. Hauser, H. Gorke, J. Ullrich, S. Herrmann, G. Schaller, F. Schopper, H. Soltau, K.-U. Kühnel, M. Messerschmidt, J. D. Bozek, S. P. Hau-Riege, M. Frank, C. Y. Hampton, R. G. Sierra, D. Starodub, G. J. Williams, J. Hajdu, N. Timneanu, M. M. Seibert, J. Andreasson, A. Rocker, O. Jönsson, M. Svenda, S. Stern, K. Nass, R. Andritschke, C.-D. Schröter, F. Krasniqi, M. Bott, K. E. Schmidt, X. Wang, I. Grotjohann, J. M. Holton, T. R. M. Barends, R. Neutze, S. Marchesini, R. Fromme, S. Schorb, D. Rupp, M. Adolph, T. Gorkhover, I. Andersson, H. Hirsemann, G. Potdevin, H. Graafsma, B. Nilsson, and J. C. H. Spence, *Nature*, 2011, **470**, 73–77.
18. J. Ullrich, A. Rudenko, and R. Moshammer, *Annu Rev Phys Chem*, 2012, **63**, 635–660.
19. A. M. Gañán-Calvo, *Phys. Rev. Lett.*, 1998, **80**, 285–288.
20. A. M. Gañán-Calvo, J. C. Lasheras, J. Davila, and A. Barrero, *Journal of Aerosol Science*, 1994, **25**, 1121–1142.
21. A. M. Gañán-Calvo, *J. Fluid Mech.*, 1997, **335**, 165–188.
22. L. Martín-Banderas, M. Flores-Mosquera, P. Riesco-Chueca, A. Rodríguez-Gil, A. Cebolla, S. Chávez, and A. M. Gañán-Calvo, *Small*, 2005, **1**, 688–692.
23. D. P. DePonte, U. Weierstall, K. Schmidt, J. Warner, D. Starodub, J. C. H. Spence, and R. B. Doak, *J. Phys. D: Appl. Phys.*, 2008, **41**, 195505.
24. R. B. Doak, D. P. DePonte, G. Nelson, F. Camacho-Alanis, A. Ros, J. C. H. Spence, and U. Weierstall, AIP, 2012, vol. 1501, pp. 1314–1323.
25. J. M. Gordillo, M. PÉREZ-SABORID, and A. M. Gañán-Calvo, *J. Fluid Mech.*, 2001, **448**.
26. A. M. Gañán-Calvo, *J. Fluid Mech.*, 2006, **553**, 75–84.
27. M. A. Herrada, A. M. Gañán-Calvo, A. Ojeda-Monge, B. Bluth, and P. Riesco-Chueca, *Phys. Rev. E*, 2008, **78**, 036323.
28. E. J. Vega, J. M. Montanero, M. A. Herrada, and A. M. Gañán-Calvo, *Phys. Fluids*, 2010, **22**, 064105.
29. J. M. Montanero, A. M. Gañán-Calvo, A. J. Acero, and E. J. Vega, *J. Micromech. Microeng.*, 2010, **20**, 075035.
30. J. M. Montanero, N. Rebollo-Muñoz, M. A. Herrada, and A. M. Gañán-Calvo, *Phys Rev E Stat Nonlin Soft Matter Phys*, 2011, **83**, 036309.
31. A. J. Acero, C. Ferrera, J. M. Montanero, and A. M. Gañán-Calvo, *J. Micromech. Microeng.*, 2012, **22**, 065011.
32. A. M. Gañán-Calvo, D. P. DePonte, M. A. Herrada, J. C. H. Spence, U. Weierstall, and R. B. Doak, *Small*, 2010, **6**, 822–824.
33. A. Aquila, M. S. Hunter, R. B. Doak, R. A. Kirian, P. Fromme, T. A. White, J. Andreasson, D. Arnlund, S. Bajt, T. R. M. Barends, M. Barthelmess, M. J. Bogan, C. Bostedt, H. Bottin, J. D. Bozek, C. Caleman, N. Coppola, J. Davidsson, D. P. DePonte, V. Elser, S. W. Epp, B. Erk, H. Fleckenstein, L. Foucar, M. Frank, R. Fromme, H. Graafsma, I. Grotjohann, L. Gumprecht, J. Hajdu, C. Y. Hampton, A. Hartmann, R. Hartmann, S. Hau-Riege, G. Hauser, H. Hirsemann, P. Holl, J. M. Holton, A. Hömke, L. Johansson, N. Kimmel, S. Kassemeyer, F. Krasniqi, K.-U. Kühnel, M. Liang, L. Lomb, E. Malmerberg, S. Marchesini, A. V. Martin, F. R. N. C. Maia, M. Messerschmidt, K. Nass, C. Reich, R. Neutze, D. Rolles, B. Rudek, A. Rudenko, I. Schlichting, C. Schmidt, K. E. Schmidt, J. Schulz, M. M. Seibert, R. L. Shoeman, R. Sierra, H. Soltau, D. Starodub, F. Stellato, S. Stern, L. Strüder, N. Timneanu, J. Ullrich, X. Wang, G. J. Williams, G. Weidenspointner, U. Weierstall, C. Wunderer, A. Barty, J. C. H. Spence, and H. N. Chapman, *Optics Express*, 2012, **20**, 2706–2716.
34. R. Neutze, R. Wouts, D. van der Spoel, E. Weckert, and J. Hajdu, *nature*, 2000, **406**, 752–757.
35. S. Boutet, L. Lomb, G. J. Williams, T. R. M. Barends, A. Aquila, R. B. Doak, U. Weierstall, D. P. DePonte, J. Steinbrener, R. L. Shoeman, M. Messerschmidt, A. Barty, T. A. White, S. Kassemeyer, R. A. Kirian, M. M. Seibert, P. A. Montanez, C. Kenney, R. Herbst, P. Hart, J. Pines, G. Haller, S. M. Gruner, H. T. Philipp, M. W. Tate, M. Hromalik, L. J. Koerner, N. van Bakel, J. Morse, W. Ghonsalves, D. Arnlund, M. J. Bogan, C. Caleman, R. Fromme, C. Y. Hampton, M. S. Hunter, L. C. Johansson, G. Katona, C. Kupitz, M. Liang, A. V. Martin, K. Nass, L. Redecke, F. Stellato, N. Timneanu, D. Wang, N. A. Zatsepin, D. Schafer, J. Defever, R. Neutze, P. Fromme, J. C. H. Spence, H. N. Chapman, and I. Schlichting, *Science*, 2012, **337**, 362–364.
36. J. Kern, R. Alonso-Mori, J. Hellmich, R. Tran, J. Hattne, H. Laksmono, C. Glockner, N. Echols, R. G. Sierra, J. Sellberg, B. Lassalle-Kaiser, R. J. Gildea, P. Glatzel, R. W. Grosse-Kunstleve, M. J. Latimer, T. A. McQueen, D. DiFiore, A. R. Fry, M. Messerschmidt, A. Miahnahri, D. W. Schafer, M. M. Seibert, D. Sokaras, T. C. Weng, P. H. Zwart, W. E. White, P. D. Adams, M. J. Bogan, S. Boutet, G. J. Williams, J. Messinger, N. K. Sauter, A. Zouni, U. Bergmann, J. Yano, and V. K. Yachandra, *PNAS*, 2012, **109**, 9721–9726.
37. A. Barty, J. Küpper, and H. N. Chapman, *Annu Rev Phys Chem*, 2013, **64**, 415–435.
38. D. A. Shapiro, H. N. Chapman, D. DePonte, R. B. Doak, P. Fromme, G. Hembree, M. Hunter, S. Marchesini, K. Schmidt, J. Spence, D. Starodub, and U. Weierstall, *J. Synchrotron Rad (2008). 15, 593-599 [doi:10.1107/S0909049508024151]*, 2008, 1–7.
39. D. P. DePonte, R. B. Doak, M. Hunter, Z. Liu, U. Weierstall, and J. C. H. Spence, *Micron*, 2009, **40**, 507–509.
40. M. Priebe, S. Kalbfleisch, M. Tolkiehn, S. Köster, B. Abel, R. J. Davies, and T. Salditt, *New J. Phys.*, 2010, **12**, 043056.
41. L. Lomb, T. Barends, S. Kassemeyer, A. Aquila, S. Epp, B. Erk, L. Foucar, R. Hartmann, B. Rudek, D. Rolles, A. Rudenko, R. Shoeman,

J. Andreasson, S. Bajt, M. Barthelmess, A. Barty, M. Bogan, C. Bostedt, J. Bozek, C. Caleman, R. Coffee, N. Coppola, D. DePonte, R. B. Doak, T. Ekeberg, H. Fleckenstein, P. Fromme, M. Gebhardt, H. Graafsma, L. Gumprecht, C. Hampton, A. Hartmann, G. Hauser, H. Hirsemann, P. Holl, J. Holton, M. Hunter, W. Kabsch, N. Kimmel, R. Kirian, M. Liang, F. R. N. Maia, A. Meinhart, S. Marchesini, A. Martin, K. Nass, C. Reich, J. Schulz, M. M. Seibert, R. Sierra, H. Soltau, J. C. Spence, J. Steinbrener, F. Stellato, S. Stern, N. Timneanu, X. Wang, G. Weidenspointner, U. Weierstall, T. White, C. Wunderer, H. Chapman, J. Ullrich, L. Strüder, and I. Schlichting, *Phys. Rev. B*, 2011, **84**, 214111.

42. A. Barty, C. Caleman, A. Aquila, N. Timneanu, L. Lomb, T. A. White, J. Andreasson, D. Arnlund, S. Bajt, T. R. M. Barends, M. Barthelmess, M. J. Bogan, C. Bostedt, J. D. Bozek, R. Coffee, N. Coppola, J. Davidsson, D. P. DePonte, R. B. Doak, T. Ekeberg, V. Elser, S. W. Epp, B. Erk, H. Fleckenstein, L. Foucar, P. Fromme, H. Graafsma, L. Gumprecht, J. Hajdu, C. Y. Hampton, R. Hartmann, A. Hartmann, G. Hauser, H. Hirsemann, P. Holl, M. S. Hunter, L. Johansson, S. Kassemeyer, N. Kimmel, R. A. Kirian, M. Liang, F. R. N. C. Maia, E. Malmerberg, S. Marchesini, A. V. Martin, K. Nass, R. Neutze, C. Reich, D. Rolles, B. Rudek, A. Rudenko, H. Scott, I. Schlichting, J. Schulz, M. M. Seibert, R. L. Shoeman, R. G. Sierra, H. Soltau, J. C. H. Spence, F. Stellato, S. Stern, L. Strüder, J. Ullrich, X. Wang, G. Weidenspointner, U. Weierstall, C. B. Wunderer, and H. N. Chapman, *Nature Photon*, 2011, **6**, 35–40.
43. M. S. Hunter, D. P. DePonte, D. A. Shapiro, R. A. Kirian, X. Wang, D. Starodub, S. Marchesini, U. Weierstall, R. B. Doak, J. C. H. Spence, and P. Fromme, *Biophys. J* ., 2011, **100**, 198–206.
44. U. Weierstall, J. C. H. Spence, and R. B. Doak, *Rev. Sci. Instrum.*, 2012, **83**, 035108.
45. J. Kern, R. Alonso-Mori, R. Tran, J. Hattne, R. J. Gildea, N. Echols, C. Glockner, J. Hellmich, H. Laksmono, R. G. Sierra, B. Lassalle-Kaiser, S. Koroidov, A. Lampe, G. Han, S. Gul, D. DiFiore, D. Milathianaki, A. R. Fry, A. Miahnahri, D. W. Schafer, M. Messerschmidt, M. M. Seibert, J. E. Koglin, D. Sokaras, T. C. Weng, J. Sellberg, M. J. Latimer, R. W. Grosse-Kunstleve, P. H. Zwart, W. E. White, P. Glatzel, P. D. Adams, M. J. Bogan, G. J. Williams, S. Boutet, J. Messinger, A. Zouni, N. K. Sauter, V. K. Yachandra, U. Bergmann, and J. Yano, *Science*, 2013, **340**, 491–495.
46. L. Redecke, K. Nass, D. P. DePonte, T. A. White, D. Rehders, A. Barty, F. Stellato, M. Liang, T. R. M. Barends, S. Boutet, G. J. Williams, M. Messerschmidt, M. M. Seibert, A. Aquila, D. Arnlund, S. Bajt, T. Barth, M. J. Bogan, C. Caleman, T.-C. Chao, R. B. Doak, H. Fleckenstein, M. Frank, R. Fromme, L. Galli, I. Grotjohann, M. S. Hunter, L. C. Johansson, S. Kassemeyer, G. Katona, R. A. Kirian, R. Koopmann, C. Kupitz, L. Lomb, A. V. Martin, S. Mogk, R. Neutze, R. L. Shoeman, J. Steinbrener, N. Timneanu, D. Wang, U. Weierstall, N. A. Zatsepin, J. C. H. Spence, P. Fromme, I. Schlichting, M. Duszenko, C. Betzel, and H. N. Chapman, 2013.
47. T. Oroguchi and M. Nakasako, *Phys. Rev. E*, 2013, **87**, 022712.
48. T. R. M. Barends, L. Foucar, R. L. Shoeman, S. Bari, S. W. Epp, R. Hartmann, G. Hauser, M. Huth, C. Kieser, L. Lomb, K. Motomura, K. Nagaya, C. Schmidt, R. Strecker, D. Anielski, R. Boll, B. Erk, H. Fukuzawa, E. Hartmann, T. Hatsui, P. Holl, Y. Inubushi, T. Ishikawa, S. Kassemeyer, C. Kaiser, F. Koeck, N. Kunishima, M. Kurka, D. Rolles, B. Rudek, A. Rudenko, T. Sato, C. D. Schroeter, H. Soltau, L. Strueder, T. Tanaka, T. Togashi, K. Tono, J. Ullrich, S. Yase, S. Wada, M. Yao, M. Yabashi, K. Ueda, and I. Schlichting, *Acta Cryst (2013). D69 [doi:10.1107/S0907444913002448]*, 2013, 1–5.
49. U. Weierstall, R. B. Doak, J. C. H. Spence, D. Starodub, D. Shapiro, P. Kennedy, J. Warner, G. G. Hembree, P. Fromme, and H. N. Chapman, *Exp Fluids*, 2008, **44**, 675–689.
50. U. Weierstall, R. B. Doak, and J. C. H. Spence, *arXiv*, 2011, physics.ins-det.
51. J. B. Knight, A. Vishwanath, J. P. Brody, and R. H. Austin, *Phys. Rev. Lett.*, 1998, **80**, 3863–3866.
52. A. Jahn, W. N. Vreeland, M. Gaitan, and L. E. Locascio, *J. Am. Chem. Soc.*, 2004, **126**, 2674–2675.
53. C. Neils, Z. Tyree, B. Finlayson, and A. Folch, *Lab Chip*, 2004, **4**, 342–350.
54. D. S. Kim, S. H. Lee, T. H. Kwon, and C. H. Ahn, *Lab Chip*, 2005, **5**, 739.
55. N. Pamme, *Lab Chip*, 2007, **7**, 1644.
56. T. Franke, A. R. Abate, D. A. Weitz, and A. Wixforth, *Lab Chip*, 2009, **9**, 2625.
57. J.-C. Baret, O. J. Miller, V. Taly, M. Ryckelynck, A. El-Harrak, L. Frenz, C. Rick, M. L. Samuels, J. B. Hutchison, J. J. Agresti, D. R. Link, D. A. Weitz, and A. D. Griffiths, *Lab Chip*, 2009, **9**, 1850.
58. A. R. Abate, J. J. Agresti, and D. A. Weitz, *Appl. Phys. Lett.*, 2010, **96**, 203509.
59. D. R. Gossett, W. M. Weaver, A. J. Mach, S. C. Hur, H. T. K. Tse, W. Lee, H. Amini, and D. Di Carlo, *Anal Bioanal Chem*, 2010, **397**, 3249–3267.
60. S.-H. Chao, M. R. Holl, J. H. Koschwanez, R. H. Carlson, L.-S. Jang, and D. R. Meldrum, *Microfluid Nanofluid*, 2005, **1**, 155–160.
61. H. Zhang, C. H. Chon, X. Pan, and D. Li, *Microfluid Nanofluid*, 2009, **7**, 739–749.
62. H. Song, J. Tice, and R. Ismagilov, *Angewandte Chemie (International ed. in English)*, 2003, **42**, 768.
63. M. Seo, Z. Nie, S. Xu, M. Mok, P. C. Lewis, R. Graham, and E. Kumacheva, *Langmuir*, 2005, **21**, 11614–11622.
64. W. Li, E. W. K. Young, M. Seo, Z. Nie, P. Garstecki, C. A. Simmons, and E. Kumacheva, *Soft Matter*, 2008, **4**, 258.
65. H. C. Shum, A. R. Abate, D. Lee, A. R. Studart, B. Wang, C.-H. Chen, J. Thiele, R. K. Shah, A. Krummel, and D. A. Weitz, *Macromol. Rapid Commun.*, 2009, NA–NA.
66. J. Thiele, A. R. Abate, H. C. Shum, S. Bachtler, S. Förster, and D. A. Weitz, *Small*, 2010, **6**, 1723–1727.
67. W. Li, J. Greener, D. Voicu, and E. Kumacheva, *Lab Chip*, 2009, **9**, 2715.
68. T. Thorsen, S. J. Maerkl, and S. R. Quake, *Science*, 2002, **298**, 580–584.
69. J. W. Hong and S. R. Quake, *Nature biotechnology*, 2003, **21**, 1179–1183.
70. J. W. Hong, V. Studer, G. Hang, W. F. Anderson, and S. R. Quake, *Nature biotechnology*, 2004, **22**, 435–439.
71. J. Melin and S. R. Quake, *Annual review of biophysics and biomolecular structure*, 2007, **36**, 213–231.
72. A. J. deMello, *Nature*, 2006, **442**, 394–402.
73. C. L. Hansen, E. Skordalakes, J. M. Berger, and S. R. Quake, *Proceedings of the National Academy of Sciences*, 2002, **99**, 16531.
74. A. Otten, S. Köster, B. Struth, A. Snigirev, and T. Pfohl, *J Synchrotron Rad*, 2005, **12**, 745–750.
75. R. Barrett, M. Faucon, J. Lopez, G. Cristobal, F. Destremaut, A. Dodge, P. Guillot, P. Laval, C. Masselon, and J.-B. Salmon, *Lab Chip*, 2006, **6**, 494–499.
76. H. M. Evans, R. Dootz, S. Koester, B. Struth, and T. Pfohl, *Bull Pol Acad Sci-Te*, 2007, **55**, 217–227.
77. R. Dootz, H. Evans, S. Köster, and T. Pfohl, *Small*, 2007, **3**, 96–100.
78. T. Pfohl, A. Otten, S. Köster, R. Dootz, B. Struth, and H. M. Evans, *Biomacromolecules*, 2007, **8**, 2167–2172.
79. J. F. Moulin, S. V. Roth, and P. Müller-Buschbaum, *Rev. Sci. Instrum.*, 2008, **79**, 015109.
80. K. N. Toft, B. Vestergaard, S. S. Nielsen, D. Snakenborg, M. G. Jeppesen, J. K. Jacobsen, L. Arleth, and J. P. Kutter, *Anal. Chem.*, 2008, **80**, 3648–3654.
81. E. Metwalli, J. F. Moulin, J. Perlich, W. Wang, A. Diethert, S. V. Roth, and P. Müller-Buschbaum, *Langmuir*, 2009, **25**, 11815–11821.
82. T. Narayanan, *Curr Opin Colloid in*, 2009.
83. H. P. Martin, N. J. Brooks, J. M. Seddon, N. J. Terrill, P. F. Luckham, A. J. Kowalski, and J. T. Cabral, *J. Phys.: Conf. Ser.*, 2010, **247**, 012050.
84. S. Köster and T. Pfohl, *Mod. Phys. Lett. B*, 2012, **26**, 1230018.
85. S. M. Taheri, S. Fischer, M. Trebbin, S. With, J. H. Schröder, J. Perlich, S. V. Roth, and S. Förster, *Soft Matter*, 2012, **8**, 12124.
86. A. Buffet, A. Rothkirch, R. Döhrmann, V. Körstgens, M. M. Abul Kashem, J. Perlich, G. Herzog, M. Schwartzkopf, R. Gehrke, P. Müller-Buschbaum, and S. V. Roth, *J. Synchrotron Rad (2012). 19, 647-653 [doi:10.1107/S0909049512016895]*, 2012, 1–7.
87. L. Daubersies, J. Leng, and J.-B. Salmon, *Lab Chip*, 2013, **13**, 910.

88. M. Trebbin, D. Steinhauser, J. Perlich, A. Buffet, S. V. Roth, W. Zimmermann, J. Thiele, and S. Förster, *PNAS*, 2013, **110**, 6706–6711.
89. B. Marmiroli, G. Grenci, F. Cacho-Nerin, B. Sartori, E. Ferrari, P. Laggner, L. Businaro, and H. Amenitsch, *Lab Chip*, 2009, **9**, 2063.
90. B. Marmiroli, G. Grenci, F. Cacho-Nerin, B. Sartori, P. Laggner, L. Businaro, and H. Amenitsch, *Nuclear Inst. and Methods in Physics Research, B*, 2010, **268**, 329–333.
91. J. Thiele, M. Windbergs, A. R. Abate, M. Trebbin, H. C. Shum, S. Förster, and D. A. Weitz, *Lab Chip*, 2011, **11**, 2362.
92. A. R. Abate, S. Seiffert, A. S. Utada, A. Shum, R. Shah, J. Thiele, W. J. Duncanson, A. Abbaspourad, M. H. Lee, and I. Akartuna, 2007.
93. G. M. Whitesides and Y. Xia, *Angew. Chem. Int. Ed.*, 1998, **37**, 550–575.
94. J.-B. Orhan, V. K. Parashar, J. Flueckiger, and M. A. M. Gijs, *Langmuir*, 2008, **24**, 9154–9161.
95. Y. Xia and G. M. Whitesides, *Annual review of materials science*, 1998, **28**, 153–184.
96. A. R. Abate, D. Lee, T. Do, C. Holtze, and D. A. Weitz, *Lab Chip*, 2008, **8**, 516.
97. P. A. Willis, B. D. Hunt, V. E. White, M. C. Lee, M. Ikeda, S. Bae, M. J. Pelletier, and F. J. Grunthaner, *Lab Chip*, 2007, **7**, 1469–1474.
98. J. P. Rolland, R. M. Van Dam, D. A. Schorzman, S. R. Quake, and J. M. Desimone, *J. Am. Chem. Soc.*, 2004, **126**, 2322–2323.
99. K. Ren, W. Dai, J. Zhou, J. Su, and H. Wu, *Proceedings of the National Academy of Sciences*, 2011, **108**, 8162.
100. L. Rayleigh, *Proceedings of the London Mathematical Society*, 1879, **1**, 57–72.
101. S. J. Leib and M. E. Goldstein, *Phys. Fluids*, 1986, **29**, 952–954.
102. S. J. Leib and M. E. Goldstein, *J. Fluid Mech.*, 1986, **168**, 479–500.
103. P. Huerre and P. A. Monkewitz, *Annu. Rev. Fluid Mech.*, 1990, **22**, 473–537.
104. S. Begolo, G. Colas, J.-L. Viovy, and L. Malaquin, *Lab Chip*, 2011, **11**, 508.
105. D. C. Duffy, J. C. McDonald, O. J. A. Schueller, and G. M. Whitesides, *Anal. Chem.*, 1998, **70**, 4974–4984.
106. H. Becker and C. Gärtner, *Electrophoresis*, 2000, **21**, 12–26.
107. A. R. Abate, D. Lee, C. Holtze, A. Krummel, T. Do, and D. A. Weitz, *Functionalized glass coating for PDMS microfluidic devices*, Caister Academic Press, 2009.
108. K. A. Heyries and C. L. Hansen, *Lab Chip*, 2011, **11**, 4122.
109. H. Sasaki, H. Onoe, T. Osaki, R. Kawano, and S. Takeuchi, *Sensors and Actuators B: Chemical*, 2010, **150**, 478–482.
110. J. N. Lee, C. Park, and G. M. Whitesides, *Anal. Chem.*, 2003, **75**, 6544–6554.
111. E. Sollier, C. Murray, P. Maoddi, and D. Di Carlo, *Lab Chip*, 2011, **11**, 3752.
112. P. Wägli, A. Homsy, and N. F. de Rooij, *Sensors and Actuators B: Chemical*, 2011, **156**, 994–1001.
113. C. F. Carlborg, T. Haraldsson, K. Öberg, M. Malkoch, and W. van der Wijngaart, *Lab Chip*, 2010, **11**, 3136.
114. N. Naik, C. Courcimault, H. Hunter, J. Berg, J. Lee, K. Naeli, T. Wright, M. Allen, O. Brand, A. Glezer, and W. King, *Sensors and Actuators A: Physical*, 2007, **134**, 119–127.
115. H. P. Chou, M. A. Unger, and S. R. Quake, *Biomedical Microdevices*, 2001, **3**, 323–330.
116. M. A. Unger, H. P. Chou, T. Thorsen, A. Scherer, and S. R. Quake, *Science*, 2000, **288**, 113–116.